Structural mechanism of signal transduction between the RNA-binding domain and the PTS-regulation domain of the LicT antiterminator.

Hélène Déméné, Thierry Ducat, Karine de Guillen, Catherine Birck, Stéphane Aymerich, Michel Kochoyan, Nathalie Declerck

THE JOURNAL OF BIOLOGICAL CHEMISTRY VOL. 283, NO. 45, pp. 30838–30849, November 7, 2008

Structural Mechanism of Signal Transduction between the RNA-binding Domain and the Phosphotransferase System Regulation Domain of the LicT Antiterminator*[S]

Received for publication, August 1, 2008 Published, JBC Papers in Press, August 5, 2008, DOI 10.1074/jbc.M805955200

Hélène Déméné[‡§¶1], Thierry Ducat[‡§¶], Karine De Guillen[‡§¶], Catherine Birck[‖‡‡], Stéphane Aymerich[§§¶¶‖‖], Michel Kochoyan[‡§¶], and Nathalie Declerck[‡§¶]**

*From the [‡]CNRS UMR 5048, [§]INSERM U554, and [¶]Université Montpellier 1&2, Centre de Biochimie Structurale, 29 Rue de Navacelles, F-34090 Montpellier, [‖]CNRS UMR 7104, **INSERM U596, and [‡‡]Université Louis Pasteur, Département de Biologie et Génétique Structurales, Institut de Génétique et de Biologie Moléculaire et Cellulaire, F-67404 Illkirch CU Strasbourg, and [§§]INRA UMR1238, [¶¶]CNRS UMR2585, and [‖‖]AgroParisTech, F-78850 Thiverval-Grignon, France*

LicT belongs to a family of bacterial transcriptional antiterminators, which control the expression of sugar-metabolizing operons in response to phosphorylations by the phosphoenolpyruvate:sugar phosphotransferase system (PTS). Previous studies of LicT have revealed the structural basis of RNA recognition by the dimeric N-terminal co-antiterminator (CAT) domain on the one hand and the conformational changes undergone by the duplicated regulation domain (PRD1 and PRD2) upon activation on the other hand. To investigate the mechanism of signal transduction between the effector and regulation modules, we have undertaken the characterization of a fragment, including the CAT and PRD1 domains and the linker in-between. Comparative experiments, including RNA binding assays, NMR spectroscopy, limited proteolysis, analytical ultracentrifugation, and circular dichroism, were conducted on native CAT-PRD1 and on a constitutively active CAT-PRD1 mutant carrying a D99N substitution in PRD1. We show that in the native state, CAT-PRD1 behaves as a rather unstable RNA-binding deficient dimer, in which the CAT dimer interface is significantly altered and the linker region is folded as a trypsin-resistant helix. In the activated mutant form, the CAT-PRD1 linker becomes protease-sensitive, and the helix content decreases, and the CAT module adopts the same dimeric conformation as in isolated CAT, thereby restoring the affinity for RNA. From these results, we propose that a helix-to-coil transition in the linker acts as the structural relay triggered by the regulatory domain for remodeling the effector dimer interface. In essence, the structural mechanism modulating the LicT RNA antitermination activity is thus similar to that controlling the DNA binding activity of dimeric transcriptional regulators.

Transcription factors are usually modular proteins that perceive environmental or intracellular signals within a sensor (or signal receiver) domain, then transmit this information to an effector domain that can either inhibit or stimulate RNA polymerase activity. In most transcriptional regulators, the effector domain is a DNA- or RNA-binding domain, whose activity is modulated by conformational changes in the sensor domain occurring upon ligand binding or chemical modification such as phosphorylation. The structural basis of this signal transduction mechanism has been unveiled for a relatively small number of transcription factors, mostly DNA-binding proteins (1). Very few studies have so far provided structural details of conditional mRNA binding by transcription regulators. Among these are the tryptophan RNA-binding attenuation protein (2, 3) and the HutP antiterminator (4).

For over 2 decades, we have been studying transcriptional regulation by a family of antitermination proteins controlling the hierarchical utilization of carbohydrates in bacteria. Within this family, LicT from *Bacillus subtilis* induces the expression of the *bglS* gene and *bglPH* operons involved in the transport and metabolism of β-glucosides (5). Other well studied members of this family are *B. subtilis* SacY (6) and *Escherichia coli* BglG (7). When activated, these transcriptional regulators bind to a ribonucleotidic antiterminator (RAT)[2] sequence in targeted mRNAs and stabilize its hairpin fold. This binding prevents the formation of an overlapping terminator hairpin, which otherwise provokes the premature arrest of transcription between the promoter and the gene coding sequences (6, 8). All members of the BglG/SacY family present the same modular organization (Fig. 1*a*). RNA binding is mediated by a N-terminal co-antiterminator (CAT) domain, which can recognize specific RAT sequences and promote antitermination on its own (9). At the C terminus of CAT are linked two homologous regulation domains, PRD1 and PRD2, which are the targets of multiple phosphorylation reactions by the phosphotransferase system (PTS) on their histidines (10–12). As to LicT, phosphorylation of the PRD1 histidines by the aryl-β-glucoside-specific enzyme

* The costs of publication of this article were defrayed in part by the payment of page charges. This article must therefore be hereby marked "*advertisement*" in accordance with 18 U.S.C. Section 1734 solely to indicate this fact.

[S] The on-line version of this article (available at http://www.jbc.org) contains supplemental Figs. S1–S4.

[1] To whom correspondence should be addressed: Centre de Biochimie Structurale, 29 Rue de Navacelles, 34090 Montpellier Cedex, France. Tel.: 33-4-67-79-11; Fax: 33-4-67-79-13; E-mail: helene.demene@cbs.cnrs.fr.

[2] The abbreviations used are: RAT, ribonucleic antiterminator; BglP, aryl-β-glucoside-specific enzyme II; CAT, co-antiterminator; DTT, dithiothreitol; EMSA, electrophoresis mobility shift assay; HSQC, heteronuclear single quantum correlation; NOE, nuclear Overhauser effect; PRD, PTS regulation domain; PTS, phosphoenolpyruvate:sugar phosphotransferase system; TCEP, tris(2-chloroethyl) phosphate; RDC, residual dipolar coupling; PDB, Protein Data Bank; CSI, Chemical Shift Index.

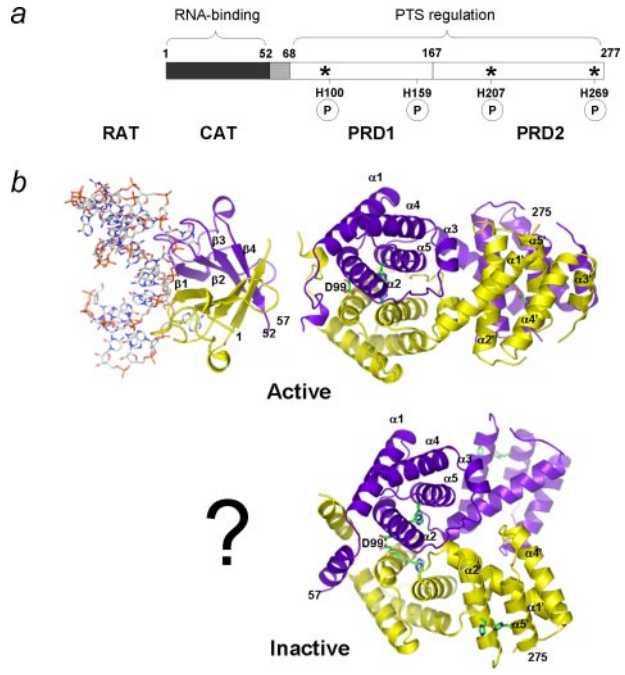

FIGURE 1. **LicT modular structure.** *a,* organization of LicT functional domains, showing the PTS-mediated phosphorylation sites (*P*) and the activating mutation sites (*). *b,* modular three-dimensional structure of LicT in its active state (*top view*) and inactive state (*bottom view*), as deduced from solution or crystal structures of different LicT constructs as follows: the active CAT dimer bound to the RAT RNA hairpin (21) (PDB 1L1C), the activated mutant form of the PTS regulation domains carrying the double H207D/H269D substitution in PRD2 (17) (PDB 1H99), and the native PTS regulation domains (18) (PDB 1TLV). The two protomers of the dimeric modules are shown in different colors. The four β-strands of the active CAT protomer and the five α-helices of the PRD1 and PRD2 bundles are labeled. The side chains of the phosphorylation/mutation sites and of Asp^{99} at the PRD1 dimeric interface are shown. The three-dimensional structures of CAT in the inactive state and of the CAT-PRD1 linker (residues 53–67) in both states are still not known.

II (BglP) inhibits antitermination, whereas phosphorylation of the PRD2 histidines by the general histidine-phosphocarrier protein leads to LicT activation and hence transcription of the *bgl* genes (12–14).

At the structural level, LicT is by far the best characterized member of the BglG/SacY antiterminator family. The three-dimensional structure of the RNA-binding domain (LicT CAT, residues 1–56) has been solved by both NMR and crystallography (15). It revealed a symmetric homodimer forming an eight-stranded β-barrel similar to that observed previously for SacY CAT (9, 16). The solution structure of LicT CAT bound to its RNA target showed that this dimeric structure remains practically unchanged upon complex formation. The first x-ray structure of a PTS regulation domain was determined for an activated mutant form of the LicT regulatory region (PRD1-PRD2, residues 57–277), in which the conserved histidines of PRD2 (His^{207} and His^{269}) had been replaced by aspartic acids to mimic phosphorylation (17). It is only more recently that the structure of the wild type regulatory region has been solved in its inactive state (18). In both the active and inactive states, LicT PRD1-PRD2 is dimeric, each PRD protomer folding as a compact five-helix bundle. The activating mutation in PRD2 causes minor changes within the protomers but a drastic rearrangement in the dimer. In the activated mutant structure, both PRD1 and PRD2 form tight dimers, whereas in the native construct most of the dimeric interface is provided by PRD1-PRD1 contacts, and PRD2 becomes almost monomeric (see Fig. 1*b*).

Although these studies clearly brought to light massive activation-dependent structural changes in the LicT regulatory region, they did not reveal how this regulation signal is transmitted from the sensor domain to the effector domain. In particular, the conformational changes undergone by CAT upon activation, as well as the structure of the CAT-PRD1 linker, remained to be determined. For this purpose, we undertook structural studies of a protein fragment containing the RNA-binding domain (CAT, residues 1–52), the first PTS regulation domain (PRD1, residues 68–167), and the intervening linker region (residues 53–67). We have previously reported a preliminary NMR characterization of the LicT CAT-PRD1, establishing its folding in a symmetrical homodimer (19). In this study, we have further characterized this construct and compared its biochemical and biophysical properties to those of a mutant CAT-PRD1 carrying a D99N substitution which, *in vivo*, renders LicT activation independent of PTS-mediated phosphorylation (20). We first demonstrate that the intrinsic ability of CAT to bind its RNA target is reduced when CAT is linked to the wild type PRD1, but it can be restored by the D99N mutation within PRD1. The conformational differences between the wild type and D99N mutant CAT-PRD1 were investigated by NMR spectroscopy, analytical ultracentrifugation, circular dichroism, and limited proteolysis experiments. The results of these analyses revealed that important rearrangements of the CAT dimeric interface are driven by PRD1, not through a direct contact between the two domains but through the helical linker, which appears to unfold upon activation. Altogether, our data provide the first structural insights into the mechanism of signal transduction between the regulatory and RNA-binding domains within an antitermination protein of the BglG/SacY family.

EXPERIMENTAL PROCEDURES

Protein Purification—The native (or wild type) CAT-PRD1 fragment (residues 1–167) and the isolated wild type PRD1 fragment (residues 57–169) were produced as 6 histidine-tagged proteins in *E. coli* BL21(DE3) and purified by affinity chromatography and size exclusion chromatography as described previously (19). The activated mutant CAT-PRD1 carrying the D99N substitution was prepared as native CAT-PRD1 except that buffer pH was raised to 7.5 during purification. The isolated CAT domain was produced as a glutathione *S*-transferase fusion protein and subsequently cleaved with thrombin (21). ^{15}N-Labeled proteins were obtained by growing cells in M9 minimal media with [^{15}N]ammonium chloride (Eurisotop, St Aubin, France) as the unique source of nitrogen. For NMR relaxation experiments, a ^{2}H-^{15}N-labeled sample of wild type CAT-PRD1 was obtained by growing a cell culture in M9 minimal media supplemented with pure $^{2}H_2O$ (SDS, Marseille, France) and [^{15}N]ammonium chloride. For the production of proteins selectively labeled with [^{15}N]Phe residues, cells were grown as described by Muchmore *et al.* (22), *i.e.* all individual amino acids, including [^{15}N]Phe, were added individually to the cell culture. Protein concentrations were measured

by the Bradford assay or by UV absorbance at 278 nm using theoretical extinction coefficients.

RNA Binding Assay—Electrophoretic mobility shift assay (EMSA) experiments were performed using a 31-base-long fluorescein-labeled oligoribonucleotide synthesized on an Applied Biosystem synthesizer and corresponding to the *bglS*-RAT target recognized by LicT (6). The experimental procedure for gel mobility shift assays was essentially the same as described before (15) except that 10 μM of fluorescein-labeled RNA was used for the binding reactions, and the fluorescent bands were revealed by UV exposure.

Fluorescence anisotropy binding assays were carried out with an Atto647N-labeled *bglS*-RAT ribonucleotide purchased from IBA (Germany). Just before use, an RNA aliquot at 200 nM was boiled for 5 min, left on ice for a few minutes, and then diluted to 2 nM in 200 mM KCl. Fluorescence anisotropy titrations were performed in Corning NBS 384-well plates by adding 40 μl of the RNA preparation to 40 μl of the purified proteins diluted in 10 mM Tris, pH 8, 150 mM NaCl, 0.5 mM EDTA, 1 mM DTT, 0.05 mg/ml bovine serum albumin. Fluorescence polarization was measured at 25 °C using a Tecan Safire fluorescence reader, and data analysis was conducted using the BIOEQS software (23).

NMR Spectroscopy—All NMR spectra were acquired on a Bruker spectrometer operating at a nominal proton frequency of 599.9 MHz and equipped with a triple resonance cryoprobe optimized for proton detection. ^{15}N-^{1}H HSQC experiments were recorded with ^{15}N and ^{1}H spectral widths of 2000 and 6000 Hz, respectively, as $t_1 \times t_2$ matrices of 64 (128) complex t_1 points × 512 (1024) complex t_2 points for CAT-PRD1 (CAT) constructs. ^{15}N-^{1}H HSQC spectra of CAT, CAT-PRD1, and D99N mutant CAT-PRD1 were recorded at 27 °C with the protein samples at 0.1 or 1 mM in 200 mM Na_2SO_4, pH 6.4, 0.5 mM EDTA, 10 mM sodium phosphate, 1 mM DTT, and 2 mM benzamidine. Titration experiments with the independent CAT and PRD1 domains were performed in the same buffer but higher pH (pH 7) to optimize PRD1 stability and solubility (19). The starting concentration of ^{15}N-CAT was 0.6 mM, and PRD1 was added up to 1.5 eq of ^{15}N-CAT (resulting in final concentrations of 0.3 and 0.45 mM, respectively). For relaxation experiments on the ^{2}H-^{15}N CAT-PRD1 protein, the buffer was 50 mM Na_2SO_4, 10 mM sodium phosphate, pH 6.4, 0.5 mM EDTA, 2 mM benzamidine. All relaxation data sets were obtained using TROSY-based pulse schemes, according to published pulse sequences (24) at 20 °C. All spectra were recorded in an interleaved manner, with a recycle delay of 2.5 s. Delay times for the $T1$ experiments were 9, 300, 600, 900, 1800, 2400, 3000, and 3600 ms, and for the $T1\rho$ experiments delay times were 3, 6, 12, 24, 30, 36, 40, and 42 ms. A 1.5-kHz ^{15}N spin-lock field was applied during the $T1\rho$ delay. Compensatory spin-lock fields were introduced in the $T1$ and $T1\rho$ experiments so that the spins experience an identical heating in all relaxation experiments. $R1$ and $R1\rho$ rates were extracted by data fitting assuming a two-parameter exponential decay, and the goodness of fit was assessed by χ^2-based statistics. $R2$ was calculated from the relationship, $R1\rho = \cos^2\theta\, R1 + \sin^2\theta\, R2$, where θ is defined as $\theta = \mathrm{artan}(\omega 1/\Omega)$, $\omega 1$ the spin lock field, and Ω the resonance offset from carrier frequency. Estimation of the diffusion tensor was done with the Tensor software from $R2/R1$ ratios (25).

Residual dipolar couplings (RDC) were calculated as the difference between splittings measured in the presence ($J+D$) and absence (J) of the alignment medium (polyethylene glycol/hexanol) (26). H_N-N coupling constants were measured as differences of splittings in the ^{15}N dimension between a regular HSQC spectrum and a TROSY spectrum recorded with 128 complex points in $F1$, and subsequently zero-filled to 256 complex points using linear forwards prediction. Extraction of the alignment tensor parameters was performed with the Module software (27).

Construction of the models was done with the InsightII software (Accelrys, Palo Alto, CA). We used the Pales software to simulate the alignment tensors and to calculate the correlation coefficients between the measured RDCs ($Jdip_{mes}$) and simulated RDCs ($Jdip_{calc}$) (28). All NMR spectra were processed with the Gifa Software (29) and analyzed with NMRview 5.0 (30).

Analytical Ultracentrifugation—Analytical ultracentrifugation experiments were performed using an Optima XL-A analytical ultracentrifuge (Beckman-Coulter, Palo Alto, CA) equipped with a UV-visible absorbance detection system. Protein preparations of native and D99N mutant CAT-PRD1 were extensively dialyzed against 50 mM $NaPO_4$ buffer, pH 7, 50 mM Na_2SO_4, 2 mM TCEP and then diluted to 0.5, 1, 2, or 4 mg/ml in the dialysis buffer. Equilibrium experiments were performed in 12-mm optical path cells by centrifugation at 8000 rpm at 5 °C until equilibrium was reached, and a final centrifugation was performed at high speed (50,000 rpm) to determine the baseline offset. Data were collected at 280 nm, and whole-cell weight average buoyant molecular weights were estimated using the software EQASSOC (31). To determine the dissociation constant of the native CAT-PRD1 dimer, sedimentation equilibrium experiments were carried out at 20 °C with a four-hole An-55 rotor and standard 1.2-cm hexa-sector cells. Samples were run at 15,000 and 18,000 rpm, and protein concentration distributions were determined at 280 nm. Sedimentation equilibrium data were fitted to a monomer-dimer model using the software SEDPHAT (32) in a global analysis of several experiments.

Far-UV Circular Dichroism Spectroscopy—After overnight dialysis in 50 mM $NaPO_4$ buffer, pH 7, 50 mM Na_2SO_4, 1 mM TCEP, protein concentration of the native and mutated LicT CAT-PRD1 preparation was measured and carefully adjusted to 0.04 mM (according to UV absorption). Far-UV spectra (180–260 nm) were recorded at room temperature, on an Applied Photophysics ChiraScan spectrometer, in a 0.1-cm path length cell at a step resolution of 1 nm. Experimental data (corresponding to a mean of five scans and corrected for background) were analyzed using four different deconvolution softwares (CDPro distribution): Lincomb (33), MLR (34), K2D (35), and Selcon3 (36). The Lincomb and MRL methods are based on fixed sets of reference proteins and are insensitive to protein concentration estimation. They thus represent the softwares of choice to perform differential analyses for native and mutants proteins to qualitatively decipher a change in secondary structures. The K2D and Selcon3 analysis software packages are known to give more reliable values of secondary structure con-

tent. Because they are sensitive to errors in the estimated protein concentrations, spectral magnitude effects had to be investigated (37), and it was found that the estimations were robust as long as the error in protein concentration was below 10%.

Limited Proteolysis—Proteins were diluted to 1 mg/ml in trypsin buffer (50 mM Tris, pH 7.5, 50 mM NaCl, 10 mM $CaCl_2$, 0.5 mM DTT), and trypsin (Sigma) was added to a final concentration of 0.01 mg/ml. The reaction was performed at 25 °C and stopped by the addition of EDTA (100 mM final concentration) and denaturating loading buffer. Proteolysis fragments were separated by electrophoresis on SDS-15% (w/v) polyacrylamide gel, electrotransferred onto nitrocellulose, and subjected to N-terminal sequencing.

RESULTS

D99N Mutation of PRD1 Restores CAT RNA Binding Activity—Previous experiments have demonstrated that the isolated CAT domain from LicT, including the 56 N-terminal residues, is able to bind to its RAT target and promote antitermination (9). In this study, we have investigated more precisely how the adjunction of the PRD1 domain modulates the RNA binding capacity of CAT *in vitro*. In EMSA experiments (Fig. 2*a*), isolated CAT produced a band shift of the RNA probe, which was already visible at a protein concentration of 0.1 μM. At this concentration, no band was detected with CAT-PRD1. This result demonstrates that the presence of the native PRD1 drastically reduces the RNA binding activity of the CAT domain.

We then investigated the effect of the D99N substitution within PRD1. This mutation, previously identified by genetic screening for PTS-independent LicT variants (22), leads to a strong constitutive active phenotype *in vivo*. In EMSA experiments, mutant D99N CAT-PRD1, in contrast with native CAT-PRD1, produced a clear band shift at a protein concentration below 0.5 μM (data not shown). A fluorescence anisotropy-based binding assay was used for quantitative comparison of protein-RNA interactions. The binding profiles observed with the wild type and D99N mutant CAT-PRD1 at 1 nM fluorescently labeled RNA (Fig. 2*b*) clearly revealed a higher affinity for the mutant protein. The dissociation constant (K_D) of the protein-RNA complex was found to be about 19 nM in case of the wild type protein and 2.6 nM in case of the mutant (see legend of Fig. 2).

Altogether our results demonstrate that the RNA binding activity of the CAT domain is reduced in the presence of the native PRD1 and that the D99N mutation within PRD1 restores efficient RNA binding, even in the absence of the PRD2 domain.

CAT Adopts a Different Conformation in the Native and Activated Mutant CAT-PRD1—NMR chemical shifts are exquisitely sensitive probes of protein conformation even in the absence of detailed three-dimensional structures. The possible conformational changes undergone by the CAT domain upon activation were investigated by this method. Fig. 3 shows the ^{15}N-^{1}H HSQC spectrum of isolated CAT (in *red*) superimposed with that of CAT-PRD1 in the native inactive form (Fig. 3*a*) or activated mutant form (Fig. 3*b*). As CAT is composed of an antiparallel β-sheet, its ^{15}N-^{1}H HSQC spectrum has very characteristic high field and down field resonances. As seen in Fig. 3*a*, many of these resonance peaks were shifted in the native

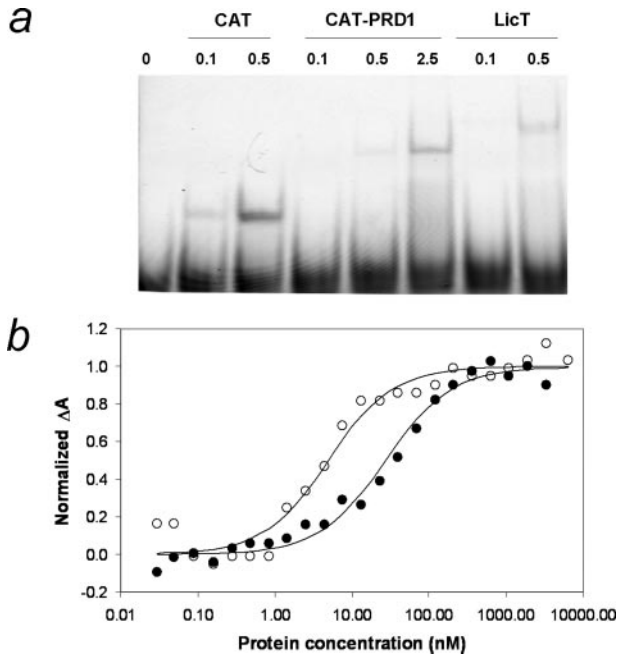

FIGURE 2. **RNA binding activity of different wild type and activated mutant LicT constructs.** *a,* electrophoretic band shift assay in 8% polyacrylamide gel with a fluorescein-labeled oligoribonucleotide (10 μM) corresponding to the *bglS*-RAT target and increasing concentrations of purified His tag proteins (μM), including different wild type or activated mutant LicT domains as follows. *a,* wild type CAT (residues 1–56), wild type CAT-PRD1 (residues 1–167), or wild type full-length LicT (CAT-PRD1-PRD2, residues 1–277). *b,* fluorescence anisotropy binding titration of Atto647N-labeled RNA probe (1 nM) with wild type (*closed circles*) or mutant LicT CAT-PRD1 (*open circles*). Normalized anisotropy changes (ΔA) are plotted as a function of protein concentration (nM); *solid line* curves correspond to data fitting using a model assuming a single binding event. Because of differences in anisotropy plateau values, probably because of differences in the dynamics of the protein-RNA complexes, we have fitted the raw data and then normalized both data and fit for comparison. The free energy of the dissociation reaction (ΔG, kcal/mol) calculated using BIOQS (23) was found to be 10.4 $\pm$ 0.9 for the wild type protein and 11.6 $\pm$ 0.3 for the mutant protein, corresponding to K_D values of about 19 and 2.6 nM, respectively. Errors were determined from rigorous 67% confidence limit testing at the 67% level.

CAT-PRD1 spectrum, indicating that the presence of the wild type PRD1 modifies the structure of CAT. In contrast, for the activated mutant CAT-PRD1, most of the peaks assigned to the RNA-binding domain could be retrieved by superposition with the NMR spectrum of isolated CAT, despite the adjunction of more than 100 additional peaks originating from PRD1. This identification was facilitated by the fact that PRD1 is an all-helix domain with the majority of its ^{15}N-^{1}H correlation peaks concentrated in the narrow and central 9–8/127–116 ppm region. Hence, 41 peaks could be readily identified as originating from the β-stranded CAT domain because their position in the mutant CAT-PRD1 spectrum remained practically unchanged. The assignments were confirmed by sequential $H_N(i)$-$H_N(i+1)$ NOE correlations found for the segments 4–5, 16–17, 18–20, 27–31, 32–35, 36–38, and 40–44, which are rich in turns. Thus, our data demonstrate that the active state of CAT is defined by a unique fold, whether it is isolated or linked to a regulatory module, whereas perturbation of this fold results in an inactive protein. Many backbone resonance shifts were also observed outside the CAT domain, indicating that important

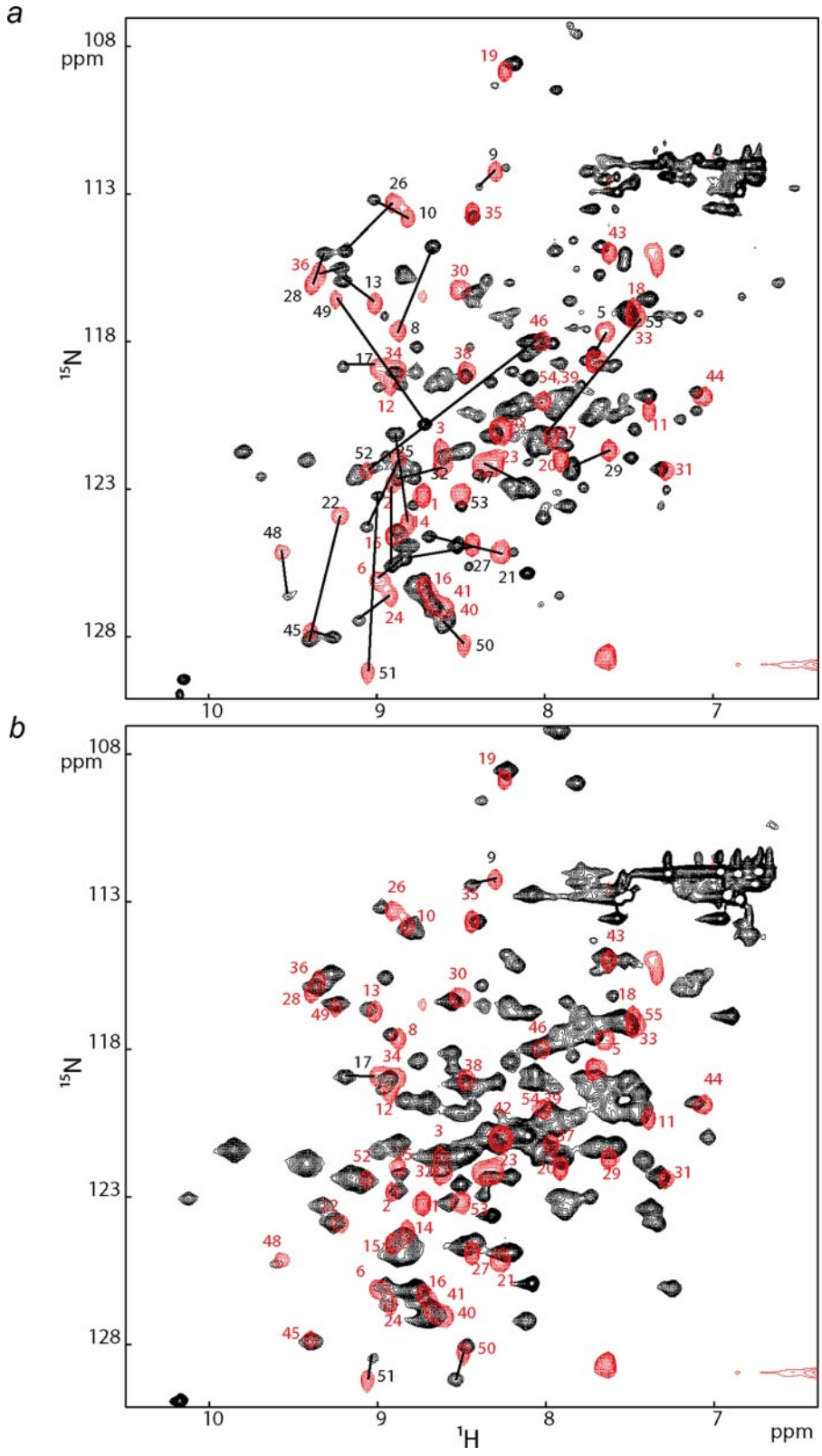

FIGURE 3. **Comparison of ^{15}N-^{1}H HSQC spectra of LicT CAT, native CAT-PRD1, and activated D99N mutant CAT-PRD1.** Heteronuclear two-dimensional NMR spectra were recorded at 27 °C with the ^{15}N-labeled proteins at 1 mM in 200 mM Na_2SO_4, pH 6.5, 2 mM DTT, 2 mM benzamidine. The figures show the spectrum of the isolated CAT domain (*red*) superimposed onto the spectrum (*black*) of native CAT-PRD1 (*a*) or activated D99N mutant CAT-PRD1 (*b*). Resonance peaks have been attributed to CAT residues based on backbone resonance assignments obtained on isolated CAT (21) or native CAT-PRD1 (19). CAT correlation peaks are numbered in *red* if not shifted and in *black* (and connected by *black lines*) if shifted. For a better comparison between spectra, the peak line width in the 13-kDa CAT spectrum has been broadened by an appropriate processing filter before Fourier transform to retrieve a comparable line width to the spectra of the 40-kDa native and mutated CAT-PRD1 constructs.

conformational changes occurred as well in the PRD1 and/or in CAT-PRD1 linker upon activation.

Interaction Mode between CAT and PRD1—The structural perturbation inflicted on CAT by native PRD1 could be due to direct contacts between the two domains. To explore this hypothesis, we produced both domains independently and performed NMR footprinting experiments using the ^{15}N-labeled CAT and the isolated nonlabeled native PRD1. Both domains were purified as dimers, as deduced from their gel filtration profile (data not shown). The ^{15}N-^{1}H HSQC spectrum of the CAT domain (0.6 mM) was found to be virtually the same in absence and in presence of 1.5 eq of PRD1 (supplemental Fig. S1). Under these conditions (c_{CAT} = 0.3 mM, c_{PRD1} = 0.45 mM), a dissociation constant of 10^{-4} M (10^{-5} M) would correspond to a concentration of 0.21 mM (0.28 mM) for the CAT-PRD1 complex. Hence, for a K_d of 10^{-4} or 10^{-5} M, we would detect changes in the NMR spectrum of CAT (either shift or broadening of resonances). The absence of changes demonstrates that CAT and PRD1 have no specific affinity for each other.

The lack of direct contact between CAT and PRD1 was also supported by the observation of slight differences in peak line widths for CAT and PRD1 in the NMR spectra of the CAT-PRD1 construct. We noticed that the resonances from CAT residues were on average 20–30% more intense than the resonances from PRD1 residues. Accordingly, the relaxation times T_1 and T_2 measured on the ^{15}N-^{2}H labeled CAT-PRD1 protein provided estimations of 29 and 32 ns for the overall correlation time (τ_c) of CAT and PRD1, respectively (at 20 °C) (supplemental Fig. S2). If the mutual orientation of the CAT and PRD1 domains was fixed, both domains would have the same correlation time of 29 ns (as predicted by Hydronmr for a closed structure obtained by combining the CAT C-terminal and PRD1 N-terminal

parts). Inversely, in the case of a complete independence, their respective correlation times would be closer to the values predicted if they were isolated, *i.e.* 8.5 and 16.4 ns for CAT and PRD1, respectively (although covalent adjunction of a domain always increases the correlation time because of steric exclusion phenomena (38, 39)). Hence, our data exclude the hypothesis where CAT and PRD1 move together as a single rigid body as well as the hypothesis where they wobble independently from each other. Rather, the correlation times are compatible with a CAT-PRD1 protein in which the two modules have no (strong) mutual interaction and are connected by a semi-rigid linker.

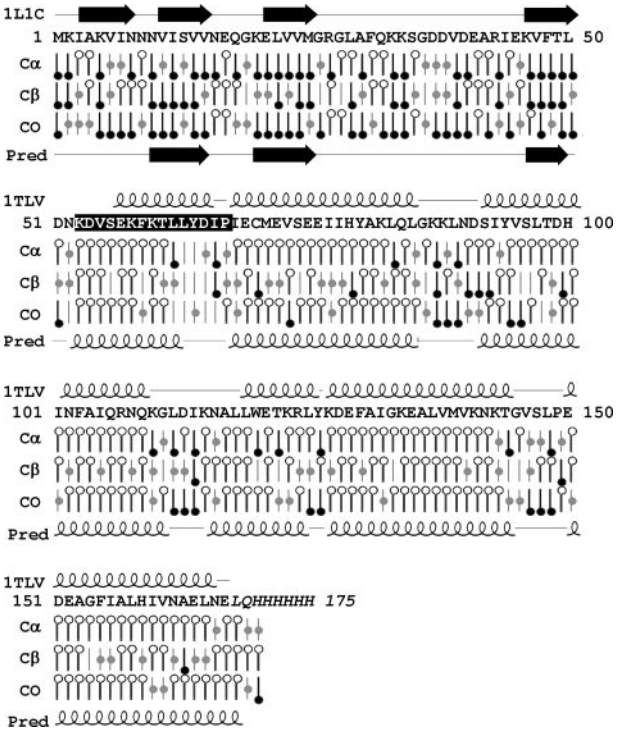

FIGURE 4. **Chemical shift index plot of the Cα, Cβ, and CO atoms and predicted secondary structure of native CAT-PRD1.** The Chemical Shift Index (*CSI*) plot of native CAT-PRD1 carbon atoms is based on the sequential resonance assignment of the triply labeled protein reported previously (19). The Chemical Shift Index plot generated using NMRview (30) is shown below the amino acid sequence of the His tag protein. On *top* and *below* are indicated the positions of β-strands (*black arrows*) and α-helices (*looped lines*) as calculated from the atomic coordinates of LicT CAT (PDB 1L1C) and native LicT regulatory domain (PDB1TLV), or as predicted (*Pred*) from the CSI plot analysis (48), respectively. The *highlighted* linker region (residues 53–67) connecting the RNA-binding domain to the regulatory domain is predicted to be folded essentially as a helix in native CAT-PRD1. For each backbone atom, Cα, Cβ, and CO, *up* and *down pins* represent positive and negative variation from the random coil chemical shifts, respectively. The reliability of secondary structure determination by CSI is estimated to be 80%. Combining CSI prediction with sequence information by the PSI-Pred software (49), whose reliability is estimated to be around 90%, confirmed the prediction of helix in the linker.

Remodeling of the CAT and PRD1 Dimer Interface—Deuteration was mandatory to achieve the assignment of the native 40-kDa LicT CAT-PRD1 protein, but precluded the recording of side chain ^{1}H-^{1}H NOEs required for structure elucidation. Although the structure of CAT in the inactive state is still unknown, valuable information on secondary and tertiary structures can be obtained from NMR experiments.

Fig. 4 shows the chemical shift index plot for backbone and Cβ carbon atoms of native LicT CAT-PRD1 based on the sequential resonance assignment of the triply labeled protein reported previously (19). The predicted secondary structure of CAT-PRD1 in the inactive state deduced from this plot indicates that at least three of the four original β-strands of the CAT monomer are present in native CAT-PRD1. Only the first strand was not correctly predicted, probably because of the particular distorted conformation of this strand. The conservation of CAT topology was confirmed by the presence of all the expected inter-strand amide-amide nuclear Overhauser effects (NOEs) as follows: Lys^{5}/Ser^{13} (β1/β2), Ile^{7}/Val^{11} (β1/β2), Val^{14}/Leu^{22} (β2/β3), Ile^{12}/Val^{24} (β2/β3), Met^{25}/Lys^{46} (β3/β4), and Val^{23}/Lys^{48} (β3/β4) NOEs (21). The conservation of the local structure of CAT was confirmed by the acceptable $\chi 2$ value obtained in the estimation of the alignment tensor parameters from the measured H_N-N RDCs and the coordinates of the x-ray structure (Table 1). The predicted secondary structures in the downstream PRD1 module were also in excellent agreement with the five-helix bundle observed in the crystal structure of the LicT regulatory region (18).

Fig. 5*A* shows that the CAT residues exhibiting the highest chemical shift variations are scattered all along the sequence. Mapping of these residues onto the three-dimensional structure (Fig. 5*B*) revealed that the perturbations correspond to the CAT dimeric interface. Moreover, in the isolated CAT dimer, the two β4 strands make antiparallel interactions, and numerous inter-strand NH/NH NOEs are observed (between residues Lys^{53}/Lys^{47}, Asn^{52}/Val^{47}, Val^{47}/Asp^{51}, and Thr^{49}/Asp^{51}). None of these inter-monomer β4/β4 NOEs was retrieved on the spectra of native CAT-PRD1, which indicates a change in the structure and/or dynamics of this β-strand. This strand is indeed the structural element where the most important chemical shift changes are measured. In addition, this β4 strand is slightly shorter in CAT-PRD1 (residues 46–50) than in isolated CAT (residues 46–53).

TABLE 1
Alignment and diffusion tensor for native CAT-PRD1

	Alignment tensor			Diffusion tensor		
	$A_{\parallel}, A_{\perp}$	α, β, γ[a]	χ^{2} [b]	$D_{\parallel}, D_{\perp}$ (10^{8} s^{-1})	α, β, γ[a]	χ^{2} [c]
CAT (native CAT-PRD1)	10.9, 3.7	−83, 114, −18	1.5	4.6, 7.7	0, 119, −23	1.4
PRD1 (native CAT-PRD1)	10.2, 4.2	118, 115, 123	2.8	ND[d]	ND	ND
CAT (D99N CAT-PRD1)	−4.2, 3	34, 92, 90	0.3[e]	ND	ND	ND

[a] Euler angles of the tensor are shown. Only the values of β and γ are meaningful for the comparison of the main axes of the diffusion and alignment tensors (α defines the orientation of the perpendicular axes).
[b] Normalized $\chi^{2} = \Sigma_i 1/N\,(J\mathrm{dip}_{\mathrm{mes}}(i) - J\mathrm{dip}_{\mathrm{calc}}(i))^{2}/\sigma^{2}(i)$.
[c] Normalized $\chi^{2} = \Sigma_i 1/N\,(R2/R1_{\mathrm{mes}}(i) - R2/R1_{\mathrm{calc}}(i))^{2}/\sigma^{2}(i)$.
[d] ND indicates not determined.
[e] The low value of normalized χ^{2} for Asp^{99} CAT-PRD1 compared with native CAT-PRD1 reflects the low values of measured RDCs.

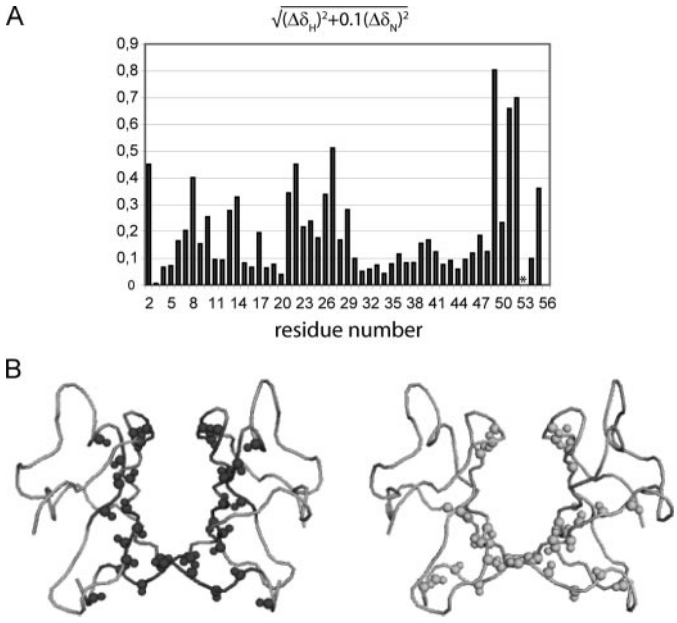

FIGURE 5. **Chemical shift differences in native CAT-PRD1 *versus* isolated CAT plotted on CAT primary and tertiary structure.** *A*, backbone chemical shift differences $(\Delta\delta_H^2+0.1\Delta\delta_N^2)^{1/2}$ measured in Fig. 2*a* are plotted as a function of the residue number in the amino sequence. The factor 0.1 normalizes the magnitude of ^{15}N chemical shift changes to that of amide ^{1}H chemical shift changes and was established from estimates of atom-specific chemical shift ranges for LicT-CAT-PRD1 (50). Resonances of residue Lys^{53} (labeled with an *asterisk*) could not be assigned. *B,* comparison of (H,N) amide couples experiencing a shift exceeding 0.2 ppm (represented as *black spheres*, *right side*) with the (H,N) amide couples of the dimer interface (represented as *light gray spheres, link side*). An (H,N) amide couple was identified as belonging to the dimer interface as soon as the H or N atom was within 5 Å of any atoms of the other protomer.

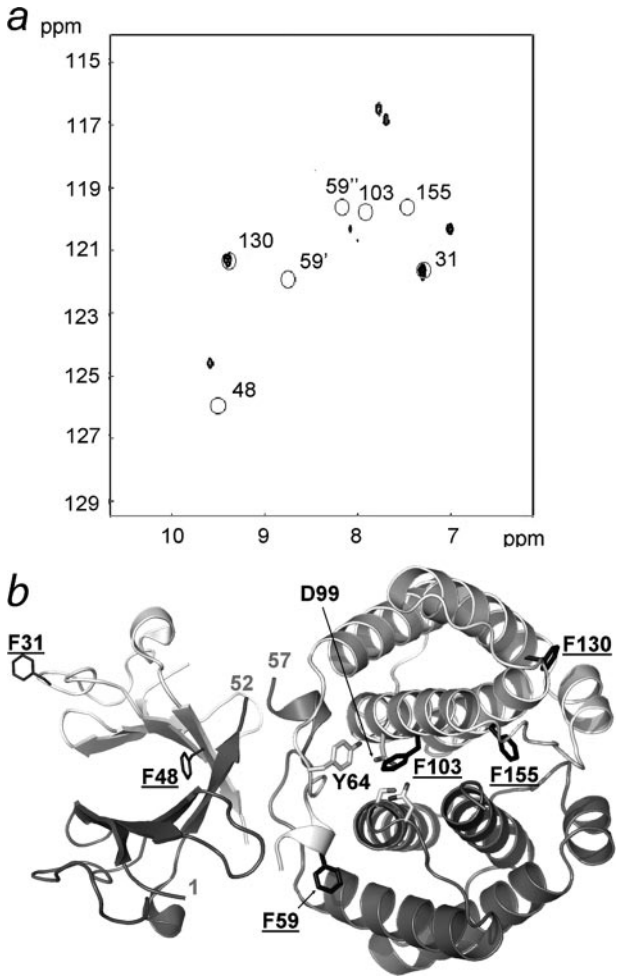

FIGURE 6. **Localization and NMR spectral characteristics of the Phe residues in D99N CAT-PRD1.** *a*, ^{1}H-^{15}N HSQC spectrum of specifically labeled ^{15}N-Phe D99N CAT-PRD1. The spectrum exhibited six correlation peaks, corresponding to Phe^{31}, Phe^{48}, Phe^{59}, Phe^{103}, Phe^{130}, and Phe^{155}. *Ellipses* indicate the positions of the corresponding correlations peaks of native CAT-PRD1 (two positions are indicated for Phe^{59}, as NMR data were ambiguous for this residue, but none corresponded to the correlation peaks found for mutant CAT-PRD1). The correlation peaks of the Phe residues belonging to the dimer interface and to the linker region are all shifted between the mutant and native protein, whereas the other Phe residues (Phe^{31} and Phe^{130}) exhibited identical NMR chemical shifts. *b*, ribbon representation of the structure of CAT and PRD1 (1H99, activated form). The side chains of the 6 Phe residues are represented in *light gray*, with their respective label *underscored*.

Our attempts to assign the ensemble of correlation peaks in the ^{15}N NMR spectra of the activated D99N CAT-PRD1 having failed, we turned to specific ^{15}N labeling of the phenylalanine residues to get further information. CAT-PRD1 contains six phenylalanines (Phe^{31}, Phe^{48}, Phe^{59}, Phe^{103}, Phe^{130}, and Phe^{155}), and the ^{15}N-^{1}H HSQC spectrum of ^{15}N-Phe D99N CAT-PRD1 exhibited indeed only six correlation peaks (Fig. 6*a*). Phe^{31} and Phe^{130} are located outside the dimer interface (Fig. 6*b*), and their correlation peaks remained unchanged between native and mutant CAT-PRD1. The Phe^{48} (CAT), Phe^{103} (PRD1), and Phe^{155} (PRD1) belong to the dimer interface of their respective module, and their correlation peak strongly shifted between native and mutant CAT-PRD1. It was also the case of Phe^{59}, located in the linker connecting CAT and PRD1, indicating a different structural environment for this residue between both protein forms.

Stabilization of the CAT-PRD1 Dimer upon Activation—As native and mutant CAT-PRD1 had different dimeric interfaces, their relative stabilities as dimers were investigated. The apparent molecular masses at different protein concentrations were first compared by analytical size exclusion chromatography. As seen in Fig. 7*a*, at a concentration of 10 mg/ml, the mutant protein eluted as a single peak in the volume expected for a 40-kDa dimer. Elution profiles of the wild type construct performed at different concentrations always exhibited the following two peaks: a 40-kDa peak, whose relative height drastically diminished as protein concentration decreased, and a mobile peak, whose position shifted toward lower molecular weight and nearly reached the value expected for the monomer (20 kDa). When concentrated and reinjected, the native protein, which was recovered from each peak, yielded the same two peak elution profile (supplemental Fig. S3). From these observations, it can be concluded that wild type CAT-PRD1 behaves as expected for a protein in dimer-monomer equilibrium (40), whereas the activated mutant protein is present as a dimer under all the conditions tested.

Analytical ultracentrifugation was then performed with both proteins at different concentrations (Table 2). The average molecular mass values measured for the mutant protein at all tested concentrations were those expected for a dimer, namely 45.1 kDa. In contrast, the apparent molecular mass values measured for native CAT-PRD1 increased from 29.6 kDa at the lowest concentration (0.5 mg/ml) to 39.1 kDa at a concentration of 4 mg/ml. Analytical ultracentrifugation experiments

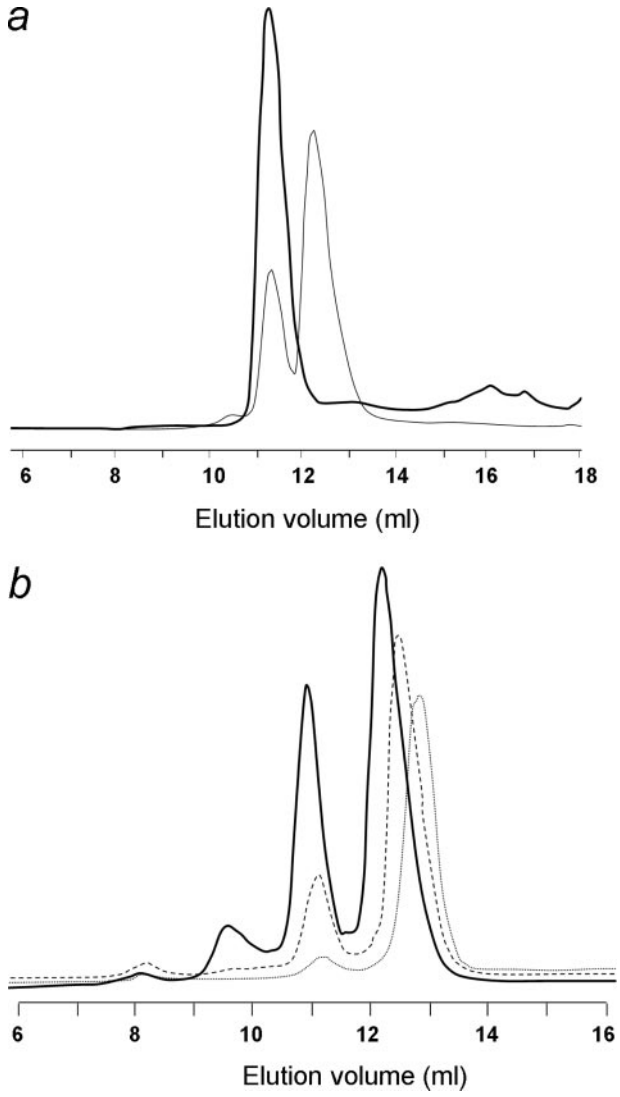

FIGURE 7. **Comparison of the elution profile of the native and activated D99N mutant CAT-PRD1 by size exclusion chromatography.** *a*, elution profile on Superdex 75 HR10/30 (GE Healthcare) of wild type (*dotted line*) and activated D99N mutant (*thick line*) CAT-PRD1 at 5 mg/ml. The mutated CAT-PRD1 protein elutes as a single peak at the position expected for a dimer of 40 kDa. The native CAT-PRD1 elutes as a double peak as follows: a minor peak corresponding to the dimer size, and a major peak corresponding to a molecular size intermediate between that of the dimeric and monomeric form. This profile is characteristic of a monomer/dimer equilibrium (40). *b,* elution profile of wild type CAT-PRD1 injected at 15 mg/ml (*solid line*), 5 mg/ml (*dashed line*), or 1 mg/ml (*dotted line*). The *height of the peak* corresponding to the dimeric form increases as the concentration of injected protein increases, as expected for a monomer-dimer equilibrium. At a concentration of 15 mg/ml, one can note the presence of minor peaks corresponding to higher molecular weight aggregates, which were not further characterized in this study.

TABLE 2

Average molar mass of wild-type and activated mutant CAT-PRD1 as determined by analytical ultracentrifugation

Protein concentration[a]	Average molar mass[b]	
	Wild-type CAT-PRD1	Active mutant CAT-PRD1 (D99N)
mg/ml		
0.5	29,600	45,150
1	31,210	45,150
2	37,260	46,130
4	39,140	45,150

[a] Concentration of the protein samples used for sedimentation equilibrium at 8000 rpm.
[b] The average molar mass (M) is related to the buoyant molar mass (M^*) of the proteins determined by whole-cell measurements at 280 nm of the concentration distribution at equilibrium. $M^* = M(1 - \nu\rho)$ where ν is the partial specific volume of the protein monomer (0.747) calculated from its amino acid sequence, and ρ is the density of the solvent.

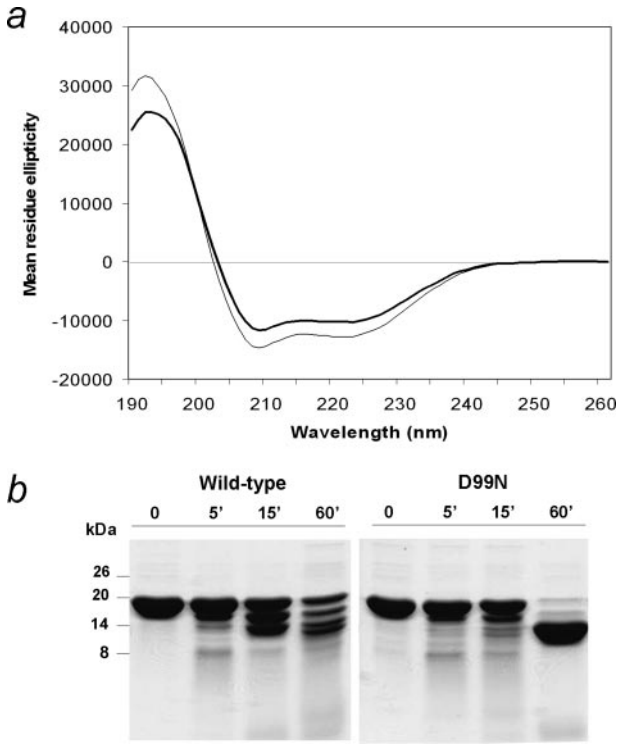

FIGURE 8. **Comparison of CD spectral properties and protease sensitivity of CAT-PRD1 in the active and inactive state.** *a,* normalized far-UV CD spectra obtained with the native (*thin line*) and activated D99N mutant (*thick line*) CAT-PRD1 proteins at 0.04 mM in 50 mM Na_2SO_4, 50 mM NaH_2PO_4, 1 mM TCEP, pH 7. The mean ellipticity values are in units of degrees·cm^2·dmol^{-1} residue^{-1}. *b*, SDS-PAGE analysis of the trypsinolysis kinetics of the native (*left*) and activated D99N mutant (*right*) CAT-PRD1 proteins at 1 mg/ml, incubated with trypsin (0.01 mg/ml). *Arrows* indicate fragments analyzed by N-terminal sequencing.

were repeated for wild type CAT-PRD1 to determine the apparent dissociation constant (K_d) for the monomer-dimer equilibrium (supplemental Fig. S4). Under the conditions used for the experiments, a K_d value ranging from 1.8 to 7.5 μM was determined for the wild type CAT-PRD1 dissociation.

Structure of the CAT-PRD1 Linker in the Inactive and Active State—Information on the backbone structure of the linker joining CAT to PRD1 (residues 53–68) could be retrieved from the high field NMR spectra of the triply labeled protein. From the backbone chemical shift index plot presented in Fig. 4, most of the CAT-PRD1 linker was predicted to be folded as a helix in wild type CAT-PRD1 (resonances of residues 63–66 could not be assigned). This helical fold was confirmed by the presence of numerous contiguous H_N-H_N NOEs (Val^{55}/Ser^{56}, Ser^{56}/Glu^{57}, Glu^{57}/Lys^{58}, Lys^{60}/Thr^{61}, and Thr^{61}/Leu^{62}). In contrast, the corresponding residues have been observed to be in a random coil in isolated CAT (21), with only two distant turns reminiscent of the helix evidenced in this study.

To examine the alternative conformation of the CAT-PRD1 linker, we have performed a precise analysis of the helical content of the LicT CAT-PRD1 constructs by far-UV circular dichroism. Fig. 8*a* shows a comparison of the normalized CD spectra obtained for the native and mutant CAT-PRD1. As

expected, they both exhibited the typical features of proteins containing a high proportion of α-helix, as evidenced by the marked minima of the mean residue ellipticity near 208 and 222 nm. However, the ellipticity minima of wild type CAT-PRD1 were found to be systematically more pronounced than those of the mutant CAT-PRD1. Accordingly, quantitative analysis of the spectra by four different deconvolution software packages (Table 3) revealed a systematic increase in helical content and a concomitant decrease in β-strand content for wild type CAT-PRD1 compared with the mutant protein. Based on the existing structural data, the helical content of the CAT-PRD1 construct is 50.3% if the linker is assumed to fold as a helix and 44.3% if it is assumed to be unstructured. Considering the shortening of CAT β4-strand observed in the wild type construct, the β-sheet content is predicted to decrease from 15.6% in the active state to 13.7% in the inactive state. These values are in good agreement with the values estimated from the CD spectra analysis using the K2D or Selcon3 methods, which usually provide the most reliable estimation of the secondary structure content (see "Experimental Procedures"). Hence, our results are consistent with a helix-to-coil transition in the linker and a gain in β-sheet structure in the CAT domain upon activation.

TABLE 3
Secondary structure content in native and activated mutant CAT-PRD1

Software[a]	Helix ()		β-Sheet		Others	
	Native	D99N	Native	D99N	Native	D99N
	%		%		%	
Lincomb	32	27	60	61	18	12
MLR	60	47	28	42	12	11
K2D	56	41	11	18	34	42
Selcon3	46	39	13	15	42	28

[a] Deconvolution softwares used for analyzing the native and activated D99N mutant CAT-PRD1 spectra are presented in Fig. 6*a*.

Unfolding of the CAT-PRD1 Helical Linker upon Activation—The conformational changes associated with activation were also investigated by limited proteolysis. As seen in Fig. 8*b*, very different trypsin hydrolysis kinetics were observed for the mutant and native proteins. After 60 min, the activated D99N CAT-PRD1 had been totally cleaved, giving rise to a protease-resistant fragment of about 12 kDa compatible with cleavage in the linker region. In contrast, a substantial amount of the wild type protein remained intact after 1 h of incubation with trypsin. N-terminal sequencing of the lowest molecular weight trypsinolysis fragments revealed cleavage at both Lys^{53} and Lys^{60} in case of the mutant, and at Lys^{60} in case of the wild type. As Lys^{53} and Lys^{60} are located within the CAT-PRD1 linker, it can be inferred that these residues are not readily accessible to protease attack in the wild type constructs, in good agreement with this region being folded as a helix in the wild type protein. The fact that this region becomes much more prone to proteolysis in the active state is also consistent with the linker helix undergoing partial unfolding upon activation.

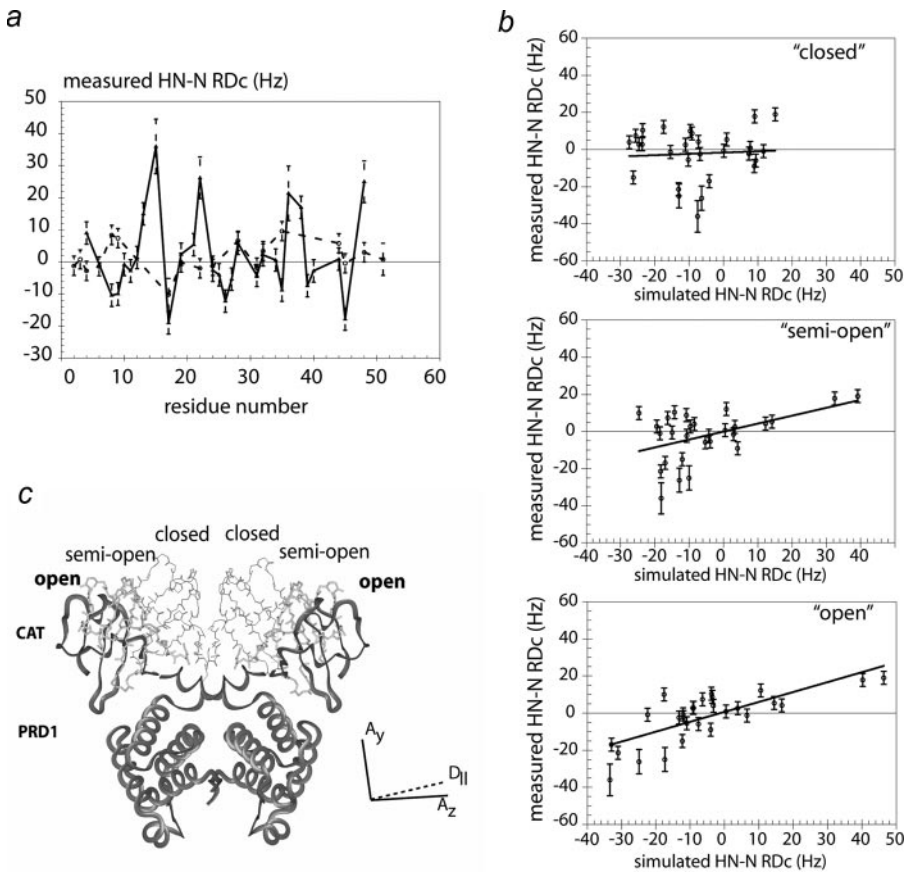

FIGURE 9. **Comparison of H_N-N RDC profiles measured for native and mutant CAT-PRD1 and simulations of different models for the native protein.** *a*, comparison of the H_N-N RDC profile measured for CAT in native and mutant D99N CAT-PRD1 as a function of the residue number in sequence. *Filled triangles,* native CAT-PRD1; *open circles,* D99N CAT-PRD1. *b*, correlation plot of experimental *versus* simulated H_N-N RDC for different models of opening of CAT represented in *c*. *c,* backbone representation of CAT in different conformers (respecting a 2-fold symmetry around the *x* axis of the derived alignment tensor). *Thin line,* closed conformation, corresponding to the top correlation plot in *b* ($r = 0.06$); *gray thick lines,* semi-open conformation, corresponding to the middle correlation plot ($r = 045$) in *b*; *dark thick line*, open conformation, corresponding to the bottom correlation plot ($r = 0.75$) in *b*. The orientation of the alignment tensor axes estimated for CAT is indicated as *solid lines* (A_x and A_z). The orientation of the main axis of the diffusion tensor of CAT assuming an axial model of tumbling is depicted as *dotted line* ($D_{||}$).

Structural Models of Native and Mutant CAT-PRD1 from H_N-N RDCs—Finally, we performed H_N-N RDC (Jdip) measurements on both proteins in a polyethylene ($C_{12}E_5$)/hexanol mixture (26). Fig. 9*a* depicts the comparison of the RDC profiles for CAT in native and mutant CAT-PRD1. Two major differences were evident; the amplitudes and signs of the couplings were strikingly different between both proteins. The D_2O splitting was 10.5 and 11.7 Hz for native and mutant proteins, respectively, indicating a similar degree of medium alignment in the spectrometer field. Hence, the difference in amplitude indicates a significant difference in

the anisotropy and tumbling mode of proteins, with CAT adopting a more isotropic tumbling in the mutant protein. In fact, in a PEG medium characterized by a D_2O splitting of 7 Hz, no RDC could be measured for D99N CAT-PRD1, whereas alignment was still detectable for native CAT-PRD1 at a D_2O splitting of only 5.3 Hz. The second difference in the RDC profiles is the quasi-systematic inversion of sign (see residues 8, 9 and 35). Accordingly, the derived alignment tensors are very different (see Table 3). For CAT in native CAT-PRD1, this tensor corresponds to a prolate model of tumbling along a *z* axis perpendicular to the axis joining CAT and PRD1 (Fig. 9*c*). This model was confirmed by the analysis of relaxation data of CAT using the Tensor software, which found a diffusion axis adopting a quasi-identical orientation (Table 1). Such an orientation was not expected if one assumes a closed model of CAT-PRD1 obtained by linking the C- and N-terminal parts of CAT and PRD1. To verify this point, we have constructed models of CAT-PRD1, where CAT adopts different orientations from a tight closed dimer to a quasi-monomeric form. We simulated the alignment tensor corresponding to these structures and the derived RDCs. Fig. 9*c* represents the correlation between experimental and simulated RDCs for three representative models. The "closed" forms of CAT all resulted in very bad correlations, with negative or null coefficients. Opening the CAT dimer, as in the "semi-closed" orientation in Fig. 9*c*, increased the correlation coefficient to 0.5. Further opening of CAT ("open" conformation in Fig. 9*c*) gave a very good correlation coefficient of 0.75. Such data strongly suggest that the alteration of the dimer interface in CAT corresponds to a large opening of the structure.

DISCUSSION

Our previous modular studies of LicT revealed the structural basis of RNA recognition by the isolated N-terminal CAT domain on one hand, as well as the conformational changes undergone by the tandem PTS regulation domains upon activation on the other hand (15, 18, 21, 41). Here we provide the first structural insights into the mechanism of signal transduction between the regulatory domain and the RNA-binding domain.

First, we showed that adding the first PTS regulation module (PRD1) to the CAT domain led to a loss of RNA binding activity *in vitro*. This finding indicates that in the absence of PRD2, PRD1, even nonphosphorylated, directly exerts a negative control on the RNA binding ability of CAT. It explains why LicT-(1–167) corresponding to CAT-PRD1 was incapable of mediating antitermination in recombinant *B. subtilis* strains (14). Moreover, we found that the RNA binding activity of CAT-PRD1 could be restored upon introducing the D99N substitution within PRD1. This finding correlates well with the active phenotype of the corresponding mutation in full-length LicT in *B. subtilis* strains that are devoid of the PTS proteins normally required for activation (20). Interestingly, the dissociation constant estimated here for D99N CAT-PRD1 is in very good agreement with that previously determined for isolated CAT (41). Hence, although the PRD2 histidines are the site of positive control of LicT activity, activation can also be achieved by appropriate mutations in PRD1. Our results show that PRD1 alone can control the RNA binding activity of CAT. The practical consequence of this finding is that the structural basis of the control mechanism can be investigated on PRD2-truncated proteins that are amenable for NMR studies.

Second, NMR data demonstrated that the structure of the active state of CAT is essentially the same, whether it is isolated or in the presence of a regulatory domain. The dimeric interface of CAT is remodeled in the inactive structure, whereas the protomer maintains its initial topology. The NMR spectrum of the ^{15}N-Phe-labeled D99N CAT-PRD1 protein indicated that the PRD1 dimer interface is also significantly altered. This conformational rearrangement is sufficient to promote dimer destabilization, as seen by size exclusion chromatography and ultracentrifugation. The nature of this destabilization is still to investigate at the PRD1 level. The equivalent mutation (D100N) in the homologous BglG antiterminator also led to a constitutive active phenotype. Modeling studies based on the (closed) activated structure of LicT-PRDs (PDB code 1H99) suggested that the activating D100N mutation improved the geometric and electrostatic complementary score of the dimeric interface in the BglG PRD1 domain, and this result was confirmed experimentally (42). As for CAT, RDC measurements and simulations strongly suggested that CAT becomes monomeric in native CAT-PRD1, which would explain the affinity decrease toward its RAT target.

How the regulatory domain of LicT monitors the formation or disruption of an RNA-binding efficient CAT dimer is the central question addressed by this study. NMR titration experiments performed with isolated domains demonstrate that CAT does not physically interact with PRD1. The absence of extensive contacts between the functional modules is also suggested by the observation that very few conserved residues are located at the protein surface outside the dimeric interfaces or the RNA-contacting region (17, 21). NMR relaxation data excluded however a high independence of wobbling modes of both domains. The experimental correlation times of 29 and 32 ns for CAT and PRD1 are in the range calculated for the close (29 ns), semi-open (32 ns), and open (34.5 ns) structures represented in Fig. 9. The relaxation data then preferentially support a model of limited flexibility of each domain. We also provide conclusive evidence that in its native environment the linker region is indeed folded as an α-helix (Fig. 4). NMR data of the selectively ^{15}N-Phe-labeled D99N CAT-PRD1 established this helix undergoes a structural rearrangement between both proteins. The circular dichroism and limited proteolysis data suggested that it unfolds at least partially upon activation (Fig. 8). This unfolding is in keeping with the observation that the native and mutant proteins exhibit very different alignment properties. In a neutral medium such as PEG/hexanol, the alignment directly reflects the tumbling anisotropy of the protein. The very weak RDCs measured for D99N CAT-PRD1 suggest that, at variance with the native protein, CAT and PRD1 modules wobble quasi-isotropically in the mutant protein. This isotropy is consistent with a model containing an unfolded linker, where the domains do not interact with each other. The differential folding of the linker according to the activation state was already observed in the crystal structures of active and inactive LicT regulatory domains (17, 18), but because CAT was missing

and no structural data on CAT in the inactive state were then available, the functional relevance of these observations remained elusive.

What are the conformational changes within the LicT regulatory domain that promote the remodeling of the CAT-PRD1 linker and of the CAT dimer upon activation? In particular, what is the structural effect of the D99N amino acid substitution? Fig. 6*b* shows that the side chain of Asp^{99} is engaged in a dense interaction network at the PRD1-PRD1 interface of the His → Asp mutant form of LicT-PRDs (17). On one side, it makes hydrogen bond interactions with two residues, Asn^{90} and Ser^{92}, of the second PRD1 monomer, thereby contributing to dimer closure and stabilization. On the other side, it contacts two residues of the extended linker, namely Leu^{62} and Tyr^{64}. All these interactions are lost in the inactive form of LicT-PRDs. The activating effect of the D99N mutation may thus be due to an improved interaction network at the PRD1-PRD1 interface around the Asn side chain. In its closed form, PRD1 interacts with the linker, preventing its folding into helix.

Based on these observations, we propose that the helix-to-coil transition of the CAT-PRD1 linker is the structural relay triggered by the LicT regulatory domain for transmitting the activation signal to the RNA-binding domain. In wild type, inactive LicT, the presence of a semi-rigid helix in the linker would force the CAT dimer to open, preventing the recognition of the RAT hairpin. In the active state, the unfolded linker would be flexible enough to enable CAT to adopt its active state. Because a number of the linker residues are conserved within the BglG/SacY family (in particular Phe^{59}, Leu^{62}, and Leu^{63}), it is likely that the linker can also fold as a helix in other LicT-type antiterminators and secondary predictions indeed suggest the presence of a helix in the linker for all sequences (data not shown).

With this study, we have made significant progress toward the elucidation at the atomic level of the regulation process mediated by transcriptional antiterminators of the BglG/SacY family. To our knowledge, these regulatory proteins present no structural or mechanistic homology with other transcription factors that bind RNA. The regulatory mechanism we describe here is by contrast highly similar to that proposed for many prokaryotic transcriptional repressors or activators such as those from the TetR, MerR, or CRP families (for review see Ref. 1). Detailed investigations will be required for establishing to which extent other family members conform to this mechanism. Indeed, studies on transcription regulator families have often challenged established paradigms and revealed that even structurally homologous proteins, sharing homologous functions, can utilize different mechanisms of action (43–47).

Acknowledgment—Marie-Thérèse Sénégas is gratefully acknowledged for help in subcloning LicT D99-CAT-PRD1 and Silvia Zorrilla for help in fluorescence data analysis.

REFERENCES

1. Huffman, J. L., and Brennan, R. G. (2002) *Curr. Opin. Struct. Biol.* **12,** 98–106
2. Antson, A. A., Dodson, E. J., Dodson, G., Greaves, R. B., Chen, X., and Gollnick, P. (1999) *Nature* **401,** 235–242
3. McElroy, C., Manfredo, A., Wendt, A., Gollnick, P., and Foster, M. (2002) *J. Mol. Biol.* **323,** 463–473
4. Kumarevel, T., Mizuno, H., and Kumar, P. K. (2005) *Nature* **434,** 183–191
5. Schnetz, K., Stulke, J., Gertz, S., Kruger, S., Krieg, M., Hecker, M., and Rak, B. (1996) *J. Bacteriol.* **178,** 1971–1979
6. Aymerich, S., and Steinmetz, M. (1992) *Proc. Natl. Acad. Sci. U. S. A.* **89,** 10410–10414
7. Mahadevan, S., and Wright, A. (1987) *Cell* **50,** 485–494
8. Schilling, O., Herzberg, C., Hertrich, T., Vorsmann, H., Jessen, D., Hubner, S., Titgemeyer, F., and Stulke, J. (2006) *Nucleic Acids Res.* **34,** 6102–6115
9. Manival, X., Yang, Y., Strub, M. P., Kochoyan, M., Steinmetz, M., and Aymerich, S. (1997) *EMBO J.* **16,** 5019–5029
10. Postma, P. W., Lengeler, J. W., and Jacobson, G. R. (1993) *Microbiol. Rev.* **57,** 543–594
11. Stulke, J., Arnaud, M., Rapoport, G., and Martin-Verstraete, I. (1998) *Mol. Microbiol.* **28,** 865–874
12. Deutscher, J., Francke, C., and Postma, P. W. (2006) *Microbiol. Mol. Biol. Rev.* **70,** 939–1031
13. Lindner, C., Galinier, A., Hecker, M., and Deutscher, J. (1999) *Mol. Microbiol.* **31,** 995–1006
14. Tortosa, P., Declerck, N., Dutartre, H., Lindner, C., Deutscher, J., and Le Coq, D. (2001) *Mol. Microbiol.* **41,** 1381–1393
15. Declerck, N., Vincent, F., Hoh, F., Aymerich, S., and van Tilbeurgh, H. (1999) *J. Mol. Biol.* **294,** 389–402
16. van Tilbeurgh, H., Manival, X., Aymerich, S., Lhoste, J. M., Dumas, C., and Kochoyan, M. (1997) *EMBO J.* **16,** 5030–5036
17. van Tilbeurgh, H., Le Coq, D., and Declerck, N. (2001) *EMBO J.* **20,** 3789–3799
18. Graille, M., Zhou, C. Z., Receveur-Brechot, V., Collinet, B., Declerck, N., and van Tilbeurgh, H. (2005) *J. Biol. Chem.* **280,** 14780–14789
19. Ducat, T., Declerck, N., Kochoyan, M., and Demene, H. (2002) *J. Biomol. NMR* **23,** 325–326
20. Lindner, C., Hecker, M., Le Coq, D., and Deutscher, J. (2002) *J. Bacteriol.* **184,** 4819–4828
21. Yang, Y., Declerck, N., Manival, X., Aymerich, S., and Kochoyan, M. (2002) *EMBO J.* **21,** 1987–1997
22. Muchmore, D. C., McIntosh, L. P., Russell, C. B., Anderson, D. E., and Dahlquist, F. W. (1989) *Methods Enzymol.* **177,** 44–73
23. Royer, C. A., and Beechem, J. M. (1992) *Methods Enzymol.* **210,** 481–505
24. Farrow, N. A., Muhandiram, R., Singer, A. U., Pascal, S. M., Kay, C. M., Gish, G., Shoelson, S. E., Pawson, T., Forman-Kay, J. D., and Kay, L. E. (1994) *Biochemistry* **33,** 5984–6003
25. Dosset, P., Hus, J. C., Blackledge, M., and Marion, D. (2000) *J. Biomol. NMR* **16,** 23–28
26. Ruckert, M., and Otting, G. (2000) *J. Am. Chem. Soc.* **122,** 7793–7797
27. Dosset, P., Hus, J. C., Marion, D., and Blackledge, M. (2001) *J. Biomol. NMR* **20,** 223–231
28. Zweckstetter, M. (2008) *Nat. Protoc* **3,** 679–690
29. Pons, J., Malliavin, T., and Delsuc, M. (1996) *J. Biomol. NMR* **8,** 445–452
30. Johnson, B., and Brevins, R. (1994) *J. Biomol. NMR* **5,** 603–614
31. Minton, A. P. (1994) *Conservation of Signal: A New Algorithm for the Elimination of the Reference Concentration as an Independently Variable Parameter in the Analysis of Sedimentation Equilibrium*, Birkhauser Boston, Inc., Cambridge, MA
32. Vistica, J., Dam, J., Balbo, A., Yikilmaz, E., Mariuzza, R. A., Rouault, T. A., and Schuck, P. (2004) *Anal. Biochem.* **326,** 234–256
33. Perczel, A., Park, K., and Fasman, G. D. (1992) *Anal. Biochem.* **203,** 83–93
34. Yang, J. T., Wu, C. S., and Martinez, H. M. (1974) *Methods Enzymol.* **130,** 208–269
35. Andrade, M. A., Chacon, P., Merelo, J. J., and Moran, F. (1993) *Protein Eng.* **6,** 383–390
36. Sreerama, N., Venyaminov, S. Y., and Woody, R. W. (1999) *Protein Sci.* **8,** 370–380
37. Miles, A. J., Whitmore, L., and Wallace, B. A. (2005) *Protein Sci.* **14,** 368–374
38. Beglova, N., North, C. L., and Blacklow, S. C. (2001) *Biochemistry* **40,** 2808–2815
39. Spitzfaden, C., Grant, R. P., Mardon, H. J., and Campbell, I. D. (1997) *J.*

Mol. Biol. **265,** 565–579
40. Stevens, F. J., Westholm, F. A., Solomon, A., and Schiffer, M. (1980) *Proc. Natl. Acad. Sci. U. S. A.* **77,** 1144–1148
41. Declerck, N., Dutartre, H., Receveur, V., Dubois, V., Royer, C., Aymerich, S., and van Tilbeurgh, H. (2001) *J. Mol. Biol.* **314,** 671–681
42. Ben-Zeev, E., Fux, L., Amster-Choder, O., and Eisenstein, M. (2005) *J. Mol. Biol.* **347,** 693–706
43. Christen, S., Srinivas, A., Bahler, P., Zeller, A., Pridmore, D., Bieniossek, C., Baumann, U., and Erni, B. (2006) *J. Biol. Chem.* **281,** 23129–23137
44. Nowak, E., Panjikar, S., Konarev, P., Svergun, D. I., and Tucker, P. A. (2006) *J. Biol. Chem.* **281,** 9659–9666
45. Schumacher, M. A., Miller, M. C., Grkovic, S., Brown, M. H., Skurray, R. A., and Brennan, R. G. (2002) *EMBO J.* **21,** 1210–1218
46. Rhee, J. E., Sheng, W., Morgan, L. K., Nolet, R., Liao, X., and Kenney, L. J. (2008) *J. Biol. Chem.* **283,** 8664–8677
47. Perron-Savard, P., De Crescenzo, G., and Le Moual, H. (2005) *Microbiology* **151,** 3979–3987
48. Wishart, D. S., Sykes, B. D., and Richards, F. M. (1992) *Biochemistry* **31,** 1647–1651
49. McGuffin, L. J., Bryson, K., and Jones, D. T. (2000) *Bioinformatics* (*Oxf.*) **16,** 404–405
50. Farmer, B. T., II, Constantine, K. L., Goldfarb, V., Friedrichs, M. S., Wittekind, M., Yanchunas, J., Jr., Robertson, J. G., and Mueller, L. (1996) *Nat. Struct. Biol.* **3,** 995–997

Structural Mechanism of Signal Transduction between the RNA-binding Domain and the Phosphotransferase System Regulation Domain of the LicT Antiterminator

Hélène Déméné, Thierry Ducat, Karine De Guillen, Catherine Birck, Stéphane Aymerich, Michel Kochoyan and Nathalie Declerck

J. Biol. Chem. 2008, 283:30838-30849.
doi: 10.1074/jbc.M805955200 originally published online August 5, 2008
